Creation of an isolated turbulent blob fed by vortex rings

Takumi Matsuzawa, Noah P Mitchell, Stéphane Perrard, William T M Irvine

nature physics

Article

https://doi.org/10.1038/s41567-023-02052-0

Creation of an isolated turbulent blob fed by vortex rings

Received: 22 August 2022

Accepted: 5 April 2023

Published online: 11 May 2023

Check for updates

Takumi Matsuzawa [1], Noah P. Mitchell [1,3], Stéphane Perrard[1,4] & William T. M. Irvine [1,2]

Turbulence is hard to control. Many experimental methods have been developed to generate this elusive state of matter, leading to fundamental insights into its statistical and structural features as well as its onset. In all cases, however, the material boundaries of the experimental apparatus pose a challenge for understanding what the turbulence has been fed and how it would freely evolve. Here we build and control a confined state of turbulence using elemental building blocks—vortex rings. We create a stationary and isolated blob of turbulence in a quiescent environment, initiated and sustained solely by vortex rings. We assemble a full picture of its three-dimensional structure, onset, energy budget and tunability. The incoming vortex rings can be endowed with conserved quantities, such as helicity, which can then be controllably transferred to the turbulent state. Our one-eddy-at-a-time approach opens the possibility for sculpting turbulent flows much as a state of matter, placing the turbulent blob at the targeted position, localizing it and ultimately harnessing it.

Vorticity, which measures the local rotation rate of a fluid, is the building block of flow. In its absence, any fine structure in an incompressible flow decays rapidly with distance from material boundaries. Conversely, injection of vorticity can power complex bulk flows[1,2], the quintessential example being the iconic multi-scale liveliness of turbulence. Canonical methods of generating turbulence rely on the spontaneous shedding of vorticity from boundaries[3–10], be it of pipes[11–14], grids[15–18] or spinning plates[19–21]. This makes it hard to control, or have detailed knowledge of, the fabric of the injected vorticity. It also often couples the turbulence to boundaries, posing a challenge to study its unconstrained evolution. Yet, our most basic models of turbulence are cast in terms of vorticity alone, with no reference to walls.

Knowing the structure of the vorticity that feeds turbulence is fundamental to a full understanding of turbulence because it determines the inviscid invariants including the amount of energy, helicity, linear impulse and angular impulse that are injected into the turbulence. The balance of the latter two invariants, for example, might lead to different types of turbulence in the large scales[22], and has been proposed to rule the decay of turbulence[23–26]. To make it possible to address these fundamental questions, we set out to build and sustain an isolated region of turbulence far away from boundaries, while controlling the injection of inviscid conserved quantities and fully observing its free evolution.

Vortex loops are a natural candidate to this end. A vortex ring is readily generated by impulsively drawing water through an orifice in a tank (Fig. 1b). Seeding the water with bubbles reveals the coherent motion of the ring as it travels across the tank, carrying its 'atmosphere' as it propagates (Fig. 1c). Such a ring can, in an ideal fluid, travel infinitely far away from the boundaries. In real fluids, vortex rings eventually decay via viscous processes, or break down due to instabilities[27–29]. Nonetheless, they coherently carry their vorticity, and associated inviscid invariants, far from the boundaries that gave rise to them.

We set out to combine vortex loops like LEGO blocks, firing them together to 'print' a stationary region of turbulence in the centre of our tank (Fig. 1a). As demonstrated in iconic vortex collision experiments[30–32], recently revisited as a minimal means to understand the inertial cascade in real space[32–35], two vortex rings fired together

[1]James Franck Institute and Department of Physics, University of Chicago, Chicago, IL, USA. [2]Enrico Fermi Institute, University of Chicago, Chicago, IL, USA. [3]Present address: Kavli Institute for Theoretical Physics, University of California, Santa Barbara, CA, USA. [4]Present address: PMMH, CNRS, ESPCI Paris, Université PSL, Sorbonne Université, Université de Paris, Paris, France. e-mail: wtmirvine@uchicago.edu

https://doi.org/10.1038/s41567-023-02052-0

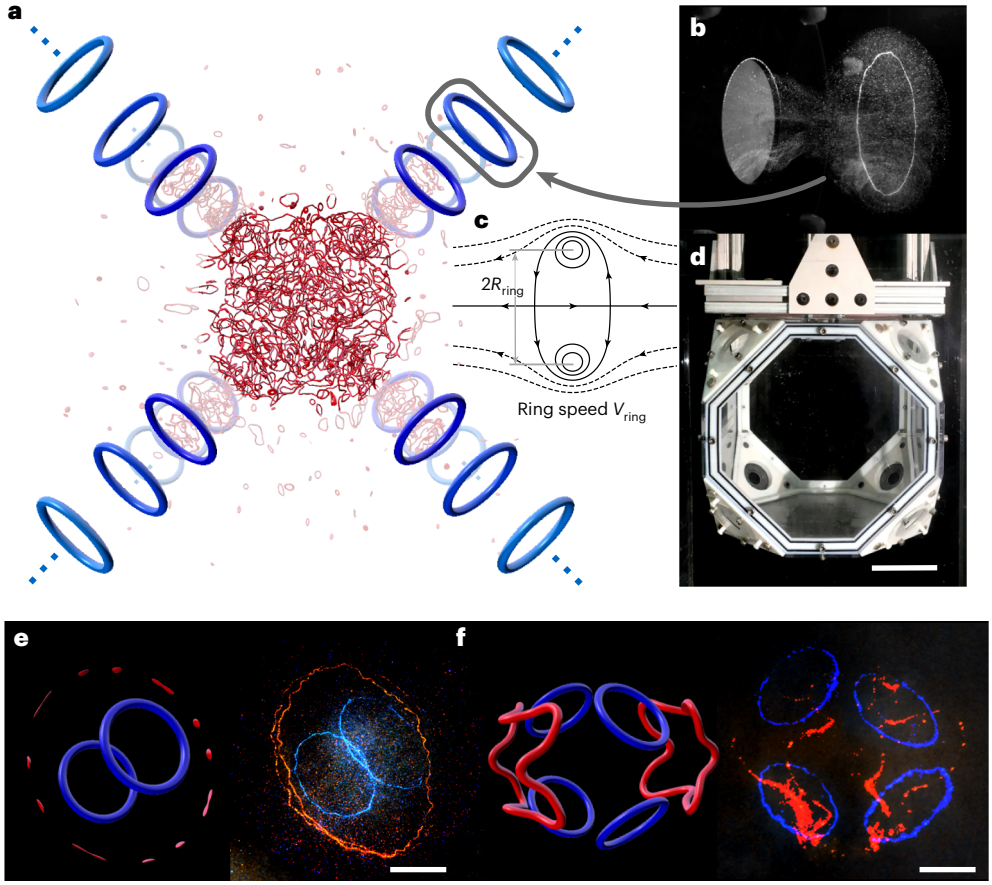

Fig. 1 | Generation of turbulence using vortex rings and their resistance to confinement. a, We envisage that colliding vortex rings creates turbulence at a target location far from boundaries with a controlled injection rate of energy. **b**, A vortex ring and its atmosphere, visualized by bubbles. **c**, Streamlines of a vortex ring in the co-moving frame. **d**, A photograph of the experimental chamber. Scale bar, 100 mm. **e**,**f**, Voriticity resists confinement, as shown by a head-on collision of two identical vortex rings (blue) generating numerous secondary rings after reconnections occur (red ellipse, which is a projection of a circle) (**e**) and a collision of four identical vortex rings resulting in two vortex loops after reconnections (red) (**f**). Left: result of a Gross–Pitaevskii simulation. Right: experimental results, visualized by bubbles. Scale bar, 30 mm along the semi-major axis of the red ellipse.

can multiply into a series of smaller rings, giving rise to turbulence. Figure 1e shows a version of this experiment using a pair of vortices created by drawing fluid into our tank through opposing orifices (Fig. 1d and Supplementary Video 1). The rings, visualized using bubbles, approach each other, stretch and recombine into smaller, outwardly propagating rings. While this example demonstrates the tendency of colliding rings to produce turbulence, it also highlights the tendency of colliding vortices to divide and redirect, escaping confinement. The situation is unchanged in the case of four (Fig. 1f) or eight (Fig. 2a–d) vortices. This generic behaviour of vortices colliding, reconnecting and escaping challenges the idea that a blob of turbulence can be printed and confined at a target position (Supplementary Video 3).

In a naïve attempt to hold the escaping vorticity in place, we fired subsequent sets of eight vortex rings at repeating intervals so that the outgoing vortices would interact with the in-going vortices. To image the flow, we use a combination of particle imaging velocimetry (PIV), seeded bubble tracking, and three-dimensional (3D) particle tracking velocimetry (PTV) (see Supplementary Section II for a detailed description of the acquisition and visualization processes). At a low frequency ($f = 0.2$ Hz), we observe a simple repetition of the single-shot reconnection dynamics (Fig. 2a–d and Supplementary Video 4), where coherent vorticity comes in and leaves (Supplementary Video 9). However, when the frequency is sufficiently high to enable the outgoing vortex rings to interact with the incoming rings, a novel state with a remarkably different vorticity distribution emerges (Fig. 2e–g and Supplementary Video 2; $f = 4$ Hz).

In this new state, vorticity is confined, and evenly distributed within an approximately spherical region (Supplementary Video 10). The flow inside the blob is in stark contrast to its surroundings, which remain relatively quiescent. The blob is sustained as long as the vortex rings are injected. Both the energy and enstrophy averaged over the measured plane indicate the comparative steadiness of the state (Fig. 2h) with weak dependence on the periodic forcing.

Figure 3a shows a Reynolds decomposition of this complex flow into mean and fluctuating components: $U_i = \langle U_i \rangle + u_i$. The blue cloud represents the average energy associated with the fluctuations and occupies the central region alone, whereas the yellow clouds represent the mean flow energy, associated with the paths along which the vortex rings are fed. We find that the flow inside the blob is dominated by fluctuations ($\langle u^2 \rangle / \langle U \rangle^2 \approx 10^{1.5}$–$10^3$) whereas the flow outside the blob is dominated by coherent flow (Supplementary Videos 5–7). Furthermore, the velocity fluctuations inside the blob are only weakly dependent on the forcing phase, whereas the coherent flow outside the blob is phase dependent, reflecting the laminar motion of the vortex rings. The temporally and radially averaged profiles of both the fluctuating energy and enstrophy are approximately constant up to a radius R_{blob} (Supplementary Section VB) but decay rapidly for $r > R_{blob}$ approximately as r^{-4}. The local dissipation rate $\epsilon_{s_{ij}}(r) = 2\nu\langle s_{ij} s_{ij} \rangle$ also possesses the same radial profile as the energy and enstrophy (Fig. 3b), where $s_{ij} = (\partial_j u_i + \partial_i u_j)/2$.

To investigate the character of the flow inside the blob, we compute the fluctuating energy spectrum and the second-order

https://doi.org/10.1038/s41567-023-02052-0

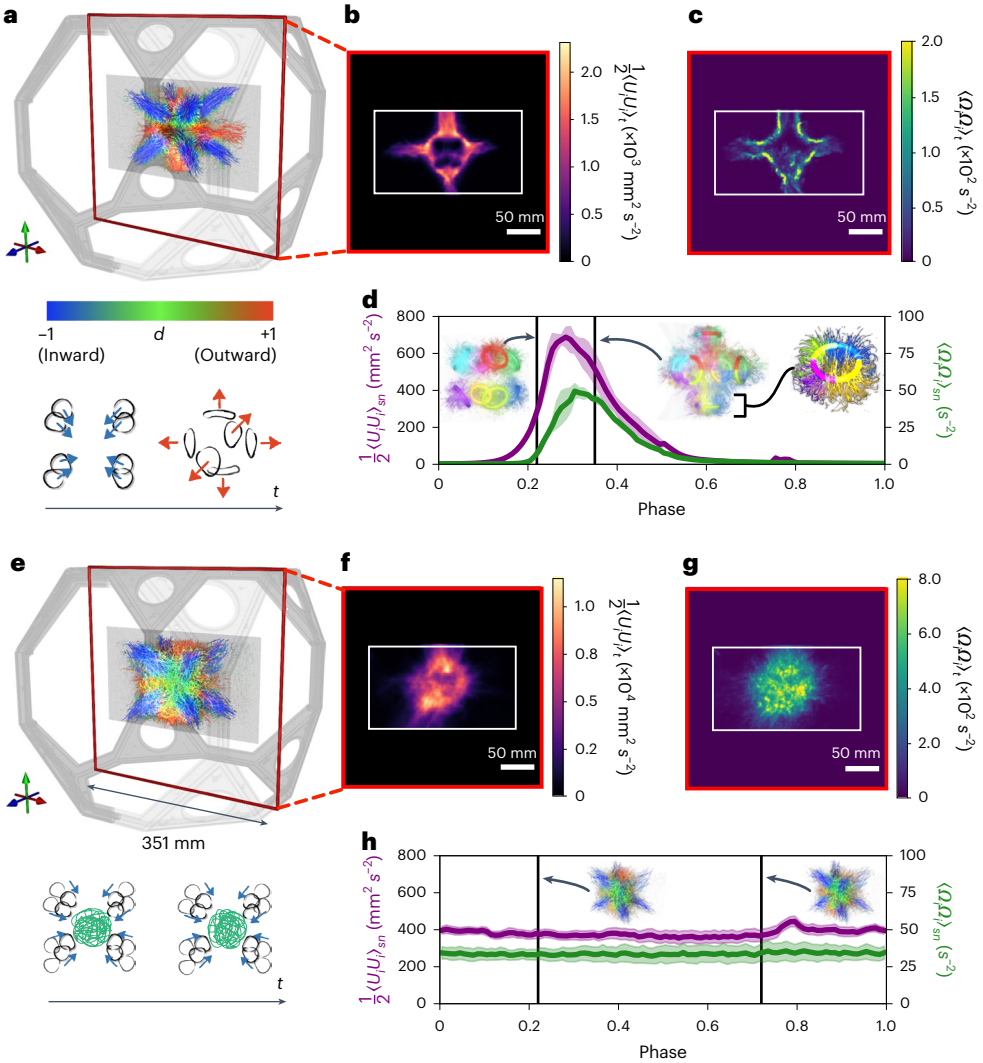

Fig. 2 | Two phases emerge as eight vortex rings repeatedly collide: coherent reconnections and a confined state of turbulence. a, Coherent vortex reconnections of eight vortex rings (blue) result in six secondary rings (red), visualized by 3D Lagrangian trajectories. The colour represents the radial component of normalized, instantaneous Lagrangian speed, $d = (\mathbf{U}_{Lag} \cdot \mathbf{r})/|\mathbf{U}_{Lag}|$. Here, $(V_{ring}/R_{ring}, f) = (20\ \text{Hz}, 0.2\ \text{Hz})$. **b**,**c**,The time-averaged energy (**b**) and the time-averaged enstrophy (**c**) on the central slice show the passage of vortex rings as they enter, reconnect and leave the central region. **d**, The spatially averaged energy and enstrophy on the central plane. Insets: 3D Lagrangian trajectories before and after the reconnections. **e**, Lagrangian trajectories around a turbulent blob display uniform, nearly isotropic outflow from the core. Here, $(V_{ring}/R_{ring}, f) = (20\ \text{Hz}, 5\ \text{Hz})$. **f**,**g**, The time-averaged energy (**f**) and the time-averaged enstrophy (**g**) show an isolated region with high energy/enstrophy. **h**, The spatially averaged energy and enstrophy show the state to be steady. Error bands in **d** and **h** represent the s.e.m. ($n = 5$ and 25 cycles, respectively). $\langle A \rangle_t$ represents the temporal average of A, and $\langle A \rangle_{sn}$ represents the phase-matched average of A over space and cycles.

structure function. PIV measurements are inherently limited at small scales by image resolution and at large scales by the finite field of view. To span the full range of scales in our turbulent flow, we performed two-dimensional (2D) PIV measurements at three levels of magnification (Fig. 3d; spatial resolutions Δ_x of 0.5, 1.3, 2.4 mm ≈ 2.4η, 6.2η, 11.4η, where η is a Kolmogorov length scale) and stitched the results together by taking into account the spectral leakage and low-pass filtering effects of PIV. With 3D PTV, we measure a one-dimensional (1D) energy spectrum on the slice that cuts the middle of the turbulent blob with a spatial resolution of $\Delta_x = 3.0\ \text{mm} = 14.4\eta$. In addition, the resulting four-dimensional (4D) velocity field affords a direct computation of a 3D energy spectrum without the assumption of isotropy (Supplementary Section VIIH). The resulting 1D energy spectrum $E_{11}(\kappa_1)$ and the second-order structure function D_{LL} of the fluctuating component of the flow are shown in Fig. 3e,f. Here κ_1 is a component of a wavenumber vector in the direction that the Fourier transform is performed. Our measurements at the three levels of magnification agree where their ranges of validity overlap. The rescaled spectrum is in agreement with the universal curve obtained by grid turbulence and turbulent boundary layer experiments[9]. Similarly, the second-order longitudinal structure function when rescaled by the 2/3 power law in the inertial sub-range is consistent with that of homogeneous isotropic turbulence.

Our spectra and structure function support the notion that the flow inside the blob is turbulent and therefore that its statistical properties can be captured by a dissipation rate ϵ_0 and an integral scale $\mathcal{L}$ (refs. 36,37), together with the fluid viscosity ν. The value of ϵ_0 is notoriously challenging to measure[38,39]. It can be inferred from the local strain rate measurements, from fitting the measured spectrum to the universal curve or by fitting the peak value in the scaled second-order structure function[38]. As discussed in Supplementary Section VIIIB, we find that all three methods are in agreement when computed on our

https://doi.org/10.1038/s41567-023-02052-0

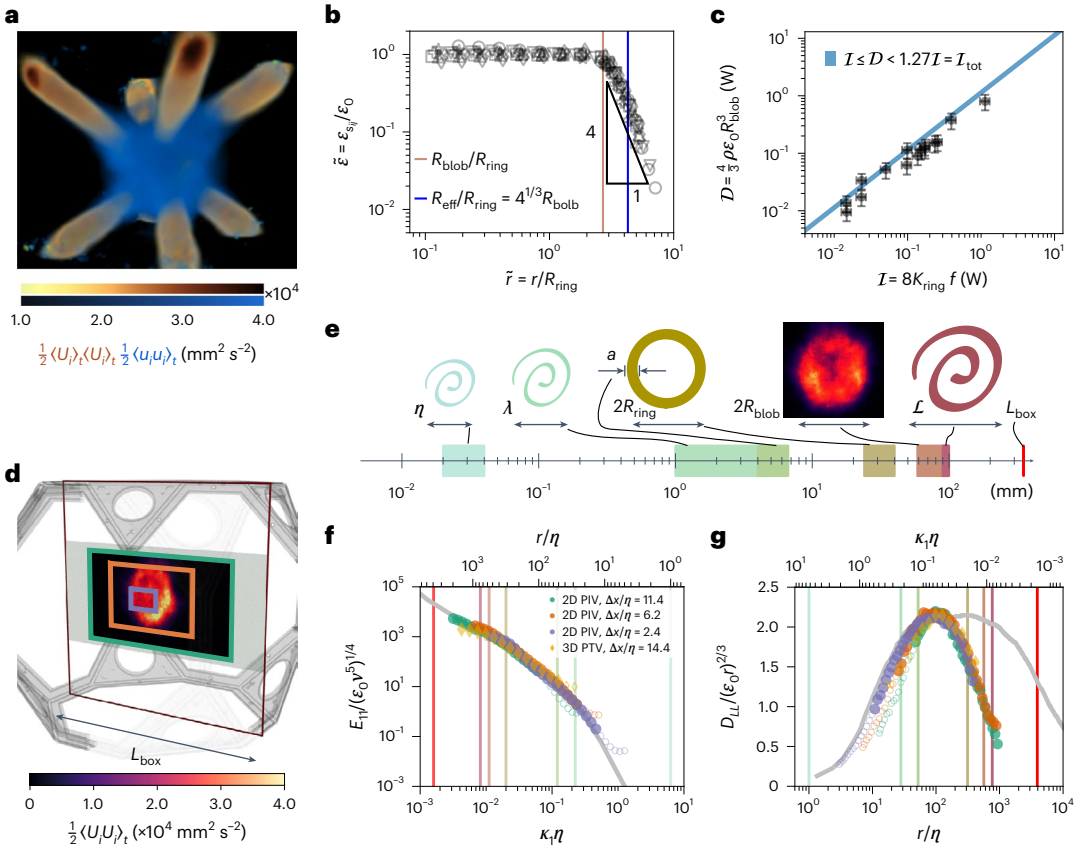

Fig. 3 | Turbulent flow statistics and energy balance in a turbulent blob. **a**, The mean flow energy $\langle U_i\rangle_t\langle U_i\rangle_t/2$ (yellow) and mean turbulent energy $\langle u_iu_i\rangle_t/2$ (blue). **b**, The radial profile of the dissipation rate on the central plane reveals a homogeneous region up to $R = R_{blob} \approx \sqrt{6}R_{ring}$ and a tail that decays with $\sim r^{-4}$. The profile collapses for rings with different radii. The parameters (Piston stroke ratio, piston effective stroke velocity, frequency) = (L/D, v_{eff} in mm s^{-1}, f in Hz) are as follows: circle (1.5, 196, 5), up-pointing triangle (2.0, 418, 5), down-pointing triangle (3.0, 443, 5), square (3.0, 443, 7), diamond (3.5, 318, 5), plus (3.5, 594, 5), diagonal cross (3.5, 594, 7), star (3.5, 594, 8). **c**, The dissipated power in the sphere of radius R_{blob} scales linearly with the power injected into the blob by the vortex rings, I. Data presented as mean ± s.e.m. (n = 12). **d**, Planes display the measurement regions of 2D PIV (i = 1, 2) at three levels of magnification. **e**, Turbulence length scales with respect to the relevant geometries (blob radius R_{blob}, ring radius R_{ring}, and core diameter a). **f**, Rescaled 1D spectra computed in the homogeneous region ($r \le R_{blob}$). Here, $\epsilon_0 = 6.0 \times 10^4$ mm^2 s^{-3}, $\nu = 1.004$ mm^2 s^{-1} and Taylor Reynolds number, $\mathrm{Re}_\lambda = 200$. λ is a Taylor microscale. The grey master curve is taken from ref. 9 ($\mathrm{Re}_\lambda \approx 600$) as a reference. κ_1 is a component of a wavenumber vector in the direction that the Fourier transform is performed. The attenuated signal due to PIV is shown by hollow data points. **g**, Rescaled second-order structure functions of the same data as in **f** shown with a reference curve from ref. 9 ($\mathrm{Re}_\lambda \approx 600$). In **f** and **g**, the turbulent length scales and relevant geometries in **e** are shown as vertical lines.

median-filtered, spatio-temporally resolved velocity fields. The corresponding value of the Kolmogorov length $\eta = (\nu^3/\epsilon_0)^{1/4}$ is shown in Fig. 3e. A measurement of the turbulent r.m.s. velocity $u' = \sqrt{\langle u_iu_i\rangle/3}$ in turn provides the estimate of the integral length scale $\mathcal{L} = u'^3/\epsilon_0$.

How are the properties of this turbulent blob controlled by the incoming vortex rings? As shown in Fig. 3e, we find the value of the integral length scale to be close to that of the blob diameter $2R_{blob}$, suggesting that both the blob radius and integral length scales are determined by the largest scale in the incoming vortex rings. This observation is supported by repetitions of our experiment in which we varied the frequency of injection of the incoming vortex rings and found no change in either $\mathcal{L}$ or R_{blob}. A repetition of our experiment in which the incoming vortex ring radius was halved instead resulted in a halving of both $\mathcal{L}$ or R_{blob} (Supplementary Section XIA).

The smallest (Kolmogorov) length scale of the turbulent blob η (Fig. 3e) has by contrast little relation to the vortex ring radius and is instead strongly affected by the incoming vortex ring energy and frequency of injection. This is consistent with the notion that, at the smallest length scales, turbulence 'forgets' about the large-scale forcing that gave rise to it and the velocity field depends on only the energy flux ϵ_0 and viscosity ν. We thus turn our attention to the balance of energy in our system.

Because the flow is at dynamical equilibrium, the dissipated power must match the power injected by the vortex rings. If we neglect any residual dissipation due to the mean flow, the energy balance is

$$4\pi\rho \int \epsilon(r) r^2 \mathrm{d}r \approx 8K_{ring}f, \quad (1)$$

where $\epsilon(r) = \epsilon_0$ if $r \le R_{blob}$ and $\epsilon_0(R_{blob}/r)^4$ otherwise. K_{ring} is the kinetic energy inside the vortex atmosphere of any one of the incoming vortices.

When integrated over all space, the left-hand side evaluates to $16/3\pi\epsilon_0R^3_{blob} = 4/3\pi\epsilon_0R^3_{eff}$, whereas if integrated up to R_{blob} we have $4/3\pi\epsilon_0R^3_{blob}$. The right-hand side requires knowledge of K_{ring}. When there is a vortex ring in a flow, the energy over all space K is generally the sum of the energy inside the vortex atmosphere K_{ring} and the energy of the added mass associated with the potential flow that surrounds the atmosphere K_{added}. K_{ring} can be further decomposed into the translational kinetic energy of the vortex atmosphere $K_{rect} = 4/3\pi R^3_{atmosphere}V^2_{ring}$ and the energy associated with the rotational motion within the vortex atmosphere K_{int}. While the exact partitioning varies by the vortex model, the variation for K_{ring} is small (<3.3%) for realistic vortex ring models. We directly measured

https://doi.org/10.1038/s41567-023-02052-0

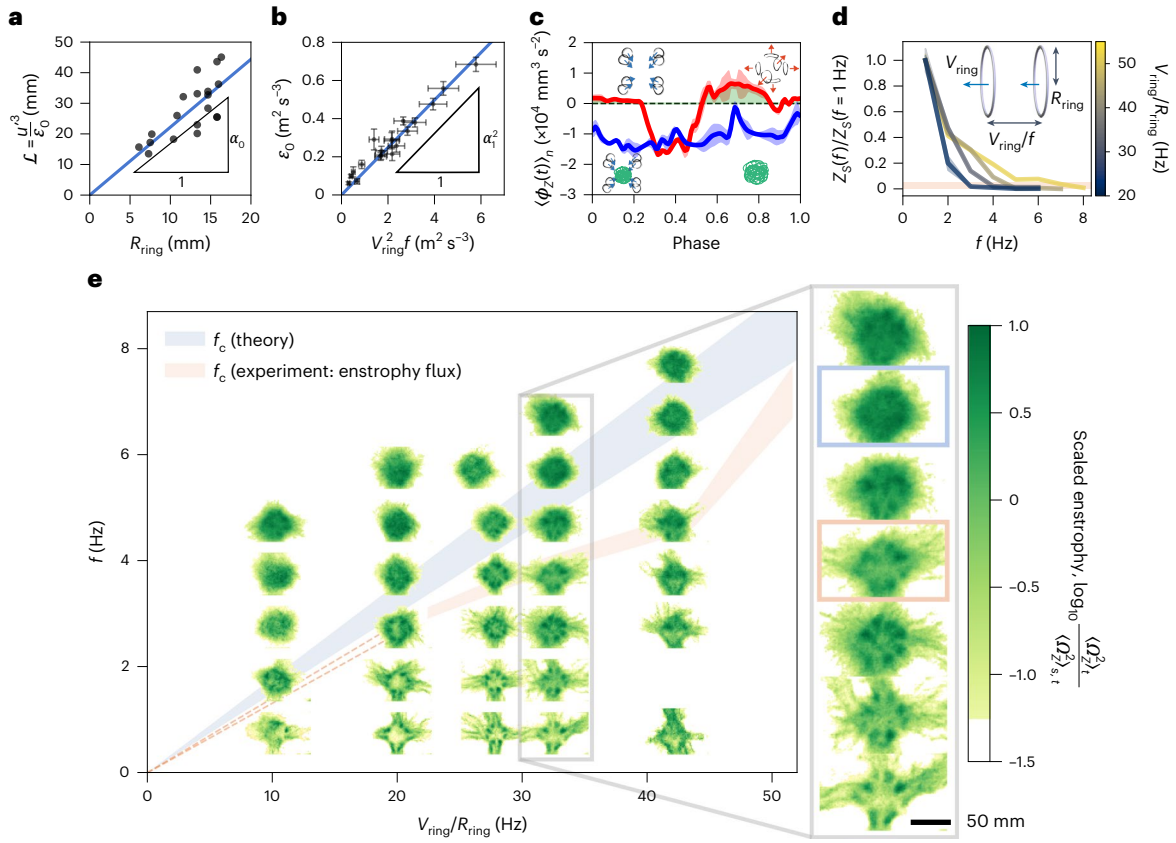

Fig. 4 | $V_{ring}/(R_{ring}f)$ governs the transition from coherent reconnections to turbulence. a, The integral length scale $\mathcal{L}$ is proportional to the radius of the injected vortex ring R_{ring}. **b**, The dissipation rate ϵ_0 inside the turbulent core is proportional to the power injected by the vortex ring ($\propto V_{ring}^2 f$). The x error bar represents the s.e.m. ($n = 5$), and the y error bar represents the s.d. of a time series of dissipation rate ($n = 500$). **c**, The phase-averaged enstrophy flux through a sphere of radius $1.9R_{blob}$ captures outgoing enstrophy below the transition (red, $f = 1$ Hz), and its absence above the transition (blue, $f = 6$ Hz) for rings with $V_{ring}/R_{ring} = 20$ Hz. Data presented as phase-locked average ± s.e.m. (red, $n = 2$; blue, $n = 10$). The insets illustrate the states of the flow in relation to the arrival of vortex rings. **d**, The scaled escaping enstrophy per cycle, $Z_s(f)/Z_s(f = 1\text{Hz})$, decreases as the injection frequency increases, indicating a transition to a blob. The orange band corresponds to <5%. The inset illustrates a geometrical relation regarding V_{ring}, R_{ring} and f. **e**, Formation of a turbulent blob depends on V_{ring}/R_{ring}. The scaled time-averaged enstrophy fields show agreements with the transition frequencies expected from our theory and measurements on the enstrophy flux. The orange band represents the frequencies at which the escaping enstrophy becomes 0–5% of the values at $f = 1$ Hz. Data presented as mean ± s.e.m. ($n = 3$).

the energy of our vortex rings and found $K_{ring} = (2.0 \pm 0.4)K_{rect}$, similar to the result of $23/14K_{rect} \approx 1.6K_{rect}$ for Hill's spherical vortex (Supplementary Section IIIC).

Figure 3c compares the measured dissipated versus injected power for a collection of blobs created by altering the ring size, speed and frequency of injection. The dissipated power scales linearly with the injected power, with a slope of approximately 1. A more granular accounting, for example, including only the energy contained within the vortex ring atmosphere and computing ϵ_0 only within R_{blob}, yields a linear relationship with lower proportionality constants: 1 (total energy, total turbulent dissipation), 0.68 (energy within the incoming vortex ring atmospheres, turbulent dissipation within a sphere of radius R_{eff}) and 0.33 (energy within the incoming vortex ring atmospheres, turbulent dissipation within a sphere of radius R_{blob}).

Crucially, increasing the velocity or frequency of injection increases the rate of energy dissipation while keeping the integral length scale fixed, thereby increasing the separation of scales $\mathcal{L}/\eta$. Thus, the ring radius and energy injection provide independent control knobs for producing turbulence of a desired intensity localized to a given region.

The picture is in stark contrast to the single-collision experiment (Fig. 2a) in which vortices come in, reconnect and go out. At these low forcing frequencies, the conversion from coherent vortex motion to turbulence is far less efficient. Even though in practice reconnections trigger energy loss within the outgoing vortices, in the limit of a single coherent collision with large separation of scales, the fraction of advected energy can be in principle 100%.

What governs the transition to a blob state? The most basic criterion is suggested by geometry: the outgoing rings will collide with the incoming rings for $f \gtrsim V_{ring}/R_{ring}$. A visualization of coherent vorticity in our flow using the Q criterion supports this hypothesis (Supplementary Video 12). A completely different conceptual approach is to seek to 'match' the incoming vortex 'eddies' to the turbulent state. A central idea in a turbulent cascade is that energy from each scale ℓ is transported to the next in a time $\tau_\ell \approx (\ell^2/\epsilon_0)^{1/3}$. If we demand that the time between incoming vortices $1/f$ match the time scale for the largest eddy to transfer energy down the cascade, we have $1/f > \tau_{\mathcal{L}}$. For our fully developed turbulent blob, we have $\mathcal{L} \propto R_{ring}$ (Fig. 4a; $\alpha_0 = 2.17 \pm 0.13$) and $\epsilon_0 \propto V_{ring}^2 f$ (Fig. 4b; $\alpha_1 = 0.35 \pm 0.02$) with proportionality constants determined in experiment. We then obtain a criterion for transition: $f_c = (\alpha_1/\alpha_0)V_{ring}/R_{ring}$ with the proportionality constant determined by the independent measurements of $\mathcal{L}(R_{ring})$ and $\epsilon_0(V_{ring})$ in the fully developed turbulent state.

Figure 4e shows the time-averaged enstrophy field for experiments in which we varied both f and V_{ring}/R_{ring}. The transitional range predicted by matching vortex arrival intervals with the largest eddy turnover time is shown by the blue band for comparison. The relationship between f_c

https://doi.org/10.1038/s41567-023-02052-0

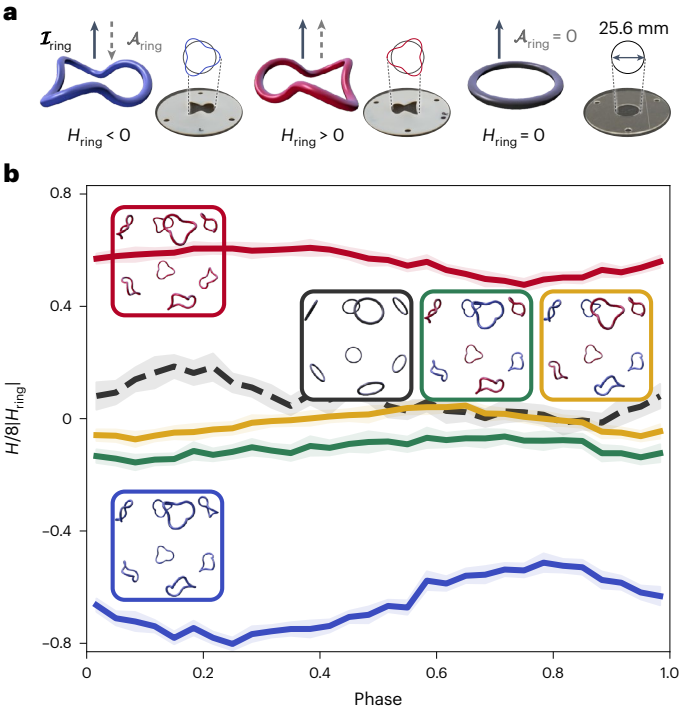

Fig. 5 | Repeated collision of helical rings transfers helicity to turbulence in a controlled fashion. a, Helical masks generate helical rings. Handedness is defined by the relative orientation of the linear impulse $\mathcal{I}_{ring}$ to the angular impulse $\mathcal{A}_{ring}$, and is tuned from anti-parallel (blue) to parallel (red). **b**, Helicity is transferred from helical rings to a blob of turbulence. Different configurations allow injection of helicity with different handedness. The five configurations of the measurements are illustrated in the insets, with (net helicity per cycle, net angular impulse per cycle) of $(8\mathcal{H}_{ring}, 0)$ (red: eight right), (0, 0) (green: four right + four left), (0, 0) (yellow: four right + four left), (0, 0) (black: eight planar) and $(-8\mathcal{H}_{ring}, 0)$ (blue: eight left). A vortex ring with $(V_{ring}/R_{ring}, f) = (40\,\text{Hz}, 5\,\text{Hz})$ was used, and the graph shows the helicity integrated over a sphere of radius 60 mm ≈ R_{blob}. The shaded band represents the s.e.m.

and V_{ring}/R_{ring}, consistent with predictions, is qualitatively visible from the change in shape as the frequency is increased. A second criterion to classify whether a given flow is in a blob state is to compute the enstrophy flux through a sphere that encloses the blob (Fig. 4c). For barotropic incompressible fluids, the integrated enstrophy flux is given by

$$\Phi_Z(t) = \int_{\partial\mathcal{V}} \Omega^2 U_i n_i \mathrm{d}S, \tag{2}$$

where $\Omega_i = \epsilon_{ijk}\partial_j U_k$ is the vorticity. Here n_i is the unit exterior normal to the surface ∂V, dS is the differential surface element, and ϵ_{ijk} is the Levi-Civita symbol. The phase-averaged (integrated) flux $\langle\Phi_Z\rangle_n$ is shown in Fig. 4c for an experiment with $f < f_c$ (red) and one with $f > f_c$ (blue). The red curve shows a trough (influx > outflux), followed by a crest (influx < outflux) as the secondary rings transport enstrophy away from the considered volume. The blue curve, by contrast, shows little to no outflux (Supplementary Video 8). As f is increased for a given V_{ring}/R_{ring}, the escaping enstrophy per cycle, Z_S, (Fig. 4c, green region) decreases smoothly as the frequency is increased (Fig. 4d). This corresponds to the suppression of coherent reconnections and development of turbulence. Placing a threshold (<5% relative to the values at $f = 1$ Hz) on the escaping enstrophy reveals that the transitional frequency depends on V_{ring}/R_{ring} in a linear fashion (Fig. 4e, orange band). The upper limit of the orange band in Fig. 4e lies within 10–20% of the predicted transition frequency.

For $f > f_c$, the energy and enstrophy are completely transferred to the blob, in sharp contrast to the single-shot experiment ($f \ll f_c$), in which neither are left behind nor in fact penetrate the central region. By contrast, the mass associated with the vortex atmospheres must flow in and out in equal amounts and cannot be left behind (Supplementary Section XA). We find it interesting that the blob state can occur in the first place given this fact. Our work raises the question of whether vortex ring trains are in some sense optimally suited to confining and 'feeding' turbulence. What types of flow 'input' lead to maximally localized blob states versus delocalized states in which the necessary outward advection destabilizes confinement?

Finally, we explore the tunability of our turbulent blob through control of the vortex rings. The ring radius R_{ring} tunes the integral scale $\mathcal{L}$ and the blob radius R_{blob}. Meanwhile, the energy balance sets the smallest scale of turbulence (the Kolmogorov scale η) as it leads to $\epsilon_0 = \alpha_1^2 V_{ring}^2 f \approx \Gamma_{ring}^2 f / R_{ring}^2$. Hence, the separation of scales is given by $\mathcal{L}/\eta \approx (\Gamma_{ring}/\nu)^{3/4}(R_{ring}f/V_{ring})^{1/4}$, consistent with the usual relation $\mathcal{L}/\eta \approx \mathrm{Re}_{\mathcal{L}}^{3/4} \approx (u'\mathcal{L}/\nu)^{3/4}$ for general turbulence[40]. Notice that it is expressed solely by the variables of the injecting vortex rings and thus can be completely controlled by tuning their properties.

Can our approach to building a turbulent blob be harnessed to endow the turbulence with additional properties? Beyond energy, natural candidates include the inviscid invariants of impulse, angular impulse and helicity. To test this possibility, we replaced the circular orifices in the corners of our tank with 3D-printed masks with helical rims. As discussed in Supplementary Section IIIC, we found that this method produces helical vortex rings that carry both angular impulse and helicity. Colliding these helical rings can in turn produce blobs with finite helicity (see Supplementary Section XIB for details). Figure 5 shows measurements of the total helicity in a blob created by colliding helical vortex loops in combinations that inject a total helicity of $+8\mathcal{H}_{ring}$, $-8\mathcal{H}_{ring}$ and $0\mathcal{H}_{ring}$, while injecting zero angular impulse and zero linear impulse. Although the vorticity field is not completely resolved (Supplementary Sections IIIC and XIB), clearly the answer is affirmative.

We have discovered that a collection of vortex rings periodically fired together leads to a self-confining turbulent blob. This bottom-up approach to turbulence provides unique design principles to position, localize and control turbulence as a state of flow. In the canonical picture of the Richardson cascade, injection and dissipation go hand in hand at dynamical equilibrium. Nevertheless, their connection often remains elusive owing to the uncontrolled injection and evolution of vortical structures. The use of coherent, controllable vortex rings overcomes this issue, enabling us to inject fully controlled arbitrary ratios of inviscid conserved quantities. Enabled by the self-confinement effect we discovered, our experiment provides a unique control of injection and dissipation in turbulence. The turbulent blob, which can be measured in its entirety and is free to evolve in isolation, offers a playground for fundamental studies on inhomogeneous turbulence such as the decay of turbulence without interference from boundaries, the response of turbulence to a periodic drive[41–47] and the role of inviscid invariants such as helicity[48,49] and angular impulse[24,25] in turbulence. The steadiness of the turbulent blob makes it an interesting alternative to boundary layers[50–54] to assess transfer at the turbulent/non-turbulent interface. Our work demonstrates how turbulence can be treated as a state of matter that can be controlled and manipulated coherently.

Online content

Any methods, additional references, Nature Portfolio reporting summaries, source data, extended data, supplementary information, acknowledgements, peer review information; details of author contributions and competing interests; and statements of data and code availability are available at https://doi.org/10.1038/s41567-023-02052-0.

References

1. Van Dyke, M. *An Album of Fluid Motion* Vol. 176 (Parabolic, 1982).
2. von Kármán, T. *Aerodynamics* Vol. 9 (McGraw-Hill, 1963).
3. Smits, A. J., McKeon, B. J. & Marusic, I. High-Reynolds number wall turbulence. *Annu. Rev. Fluid Mech.* **43**, 353–375 (2011).
4. Adrian, R. J. Hairpin vortex organization in wall turbulence. *Phys. Fluids* **19**, 041301 (2007).
5. Christensen, K. T. & Adrian, R. J. Statistical evidence of hairpin vortex packets in wall turbulence. *J. Fluid Mech.* **431**, 433–443 (2001).
6. Zhou, J., Adrian, R. J., Balachandar, S. & Kendall, T. Mechanisms for generating coherent packets of hairpin vortices in channel flow. *J. Fluid Mech.* **387**, 353–396 (1999).
7. Acarlar, M. & Smith, C. A study of hairpin vortices in a laminar boundary layer. Part 1. Hairpin vortices generated by a hemisphere protuberance. *J. Fluid Mech.* **175**, 1–41 (1987).
8. Acarlar, M. & Smith, C. A study of hairpin vortices in a laminar boundary layer. Part 2. Hairpin vortices generated by fluid injection. *J. Fluid Mech.* **175**, 43–83 (1987).
9. Saddoughi, S. G. & Veeravalli, S. V. Local isotropy in turbulent boundary layers at high reynolds number. *J. Fluid Mech.* **268**, 333–372 (1994).
10. Theodorsen, T. Mechanism of turbulence. In *Proc. Second Midwestern Conference on Fluid Mechanics* 1–19 (Ohio State Univ., 1952).
11. Reynolds, O. XXIX. An experimental investigation of the circumstances which determine whether the motion of water shall be direct or sinuous, and of the law of resistance in parallel channels. *Phil. Trans. R. Soc.* **174**, 935–982 (1883).
12. Mullin, T. Experimental studies of transition to turbulence in a pipe. *Annu. Rev. Fluid Mech.* **43**, 1–24 (2011).
13. Eckhardt, B., Schneider, T. M., Hof, B. & Westerweel, J. Turbulence transition in pipe flow. *Annu. Rev. Fluid Mech.* **39**, 447–468 (2007).
14. Hof, B., Juel, A. & Mullin, T. Scaling of the turbulence transition threshold in a pipe. *Phys. Rev. Lett.* **91**, 244502 (2003).
15. Hurst, D. & Vassilicos, J. Scalings and decay of fractal-generated turbulence. *Phys. Fluids* **19**, 035103 (2007).
16. Kistler, A. & Vrebalovich, T. Grid turbulence at large reynolds numbers. *J. Fluid Mech.* **26**, 37–47 (1966).
17. Comte-Bellot, G. & Corrsin, S. Simple eulerian time correlation of full-and narrow-band velocity signals in grid-generated, 'isotropic' turbulence. *J. Fluid Mech.* **48**, 273–337 (1971).
18. Bodenschatz, E., Bewley, G. P., Nobach, H., Sinhuber, M. & Xu, H. Variable density turbulence tunnel facility. *Rev. Sci. Instrum.* **85**, 093908 (2014).
19. de la Torre, A. & Burguete, J. Slow dynamics in a turbulent von kármán swirling flow. *Phys. Rev. Lett.* **99**, 054101 (2007).
20. Volk, R., Calzavarini, E., Leveque, E. & Pinton, J.-F. Dynamics of inertial particles in a turbulent von kármán flow. *J. Fluid Mech.* **668**, 223–235 (2011).
21. Labbé, R., Pinton, J.-F. & Fauve, S. Study of the von Kármán flow between coaxial corotating disks. *Phys. Fluids* **8**, 914–922 (1996).
22. Krogstad, P.-Å & Davidson, P. Is grid turbulence saffman turbulence? *J. Fluid Mech.* **642**, 373–394 (2010).
23. Davidson, P. *Turbulence: An Introduction for Scientists and Engineers* (Oxford Univ. Press, 2015).
24. Davidson, P. The role of angular momentum conservation in homogeneous turbulence. *J. Fluid Mech.* **632**, 329–358 (2009).
25. Saffman, P. Note on decay of homogeneous turbulence. *Phys. Fluids* **10**, 1349–1349 (1967).
26. Landau, L. D. & Lifshitz, E. M. *Fluid Mechanics: Landau and Lifshitz: Course of Theoretical Physics* Vol. 6 (Elsevier, 2013).
27. Crow, S. C. Stability theory for a pair of trailing vortices. *AIAA J.* **8**, 2172–2179 (1970).
28. Tsai, C.-Y. & Widnall, S. E. The stability of short waves on a straight vortex filament in a weak externally imposed strain field. *J. Fluid Mech.* **73**, 721–733 (1976).
29. Le Dizes, S. & Laporte, F. Theoretical predictions for the elliptical instability in a two-vortex flow. *J. Fluid Mech.* **471**, 169–201 (2002).
30. Oshima, Y. Head-on collision of two vortex rings. *J. Phys. Soc. Jpn* **44**, 328–331 (1978).
31. Lim, T. T. & Nickels, T. B. Instability and reconnection in the head-on collision of two vortex rings. *Nature* **357**, 225–227 (1992).
32. McKeown, R., Ostilla-Mónico, R., Pumir, A., Brenner, M. P. & Rubinstein, S. M. Turbulence generation through an iterative cascade of the elliptical instability. *Sci. Adv.* **6**, 2717 (2020).
33. Brenner, M. P., Hormoz, S. & Pumir, A. Potential singularity mechanism for the euler equations. *Phys. Rev. Fluids* **1**, 084503 (2016).
34. McKeown, R., Ostilla-Mónico, R., Pumir, A., Brenner, M. P. & Rubinstein, S. M. Cascade leading to the emergence of small structures in vortex ring collisions. *Phys. Rev. Fluids* **3**, 124702 (2018).
35. Ostilla-Mónico, R., McKeown, R., Brenner, M. P., Rubinstein, S. M. & Pumir, A. Cascades and reconnection in interacting vortex filaments. *Phys. Rev. Fluids* **6**, 074701 (2021).
36. Kolmogorov, A. N. The local structure of turbulence in incompressible viscous fluid for very large Reynolds numbers. *C. R. Acad. Sci. URSS* **30**, 301–305 (1941).
37. Kolmogorov, A. N. A refinement of previous hypotheses concerning the local structure of turbulence in a viscous incompressible fluid at high reynolds number. *J. Fluid Mech.* **13**, 82–85 (1962).
38. de Jong, J. et al. Dissipation rate estimation from PIV in zero-mean isotropic turbulence. *Exp. Fluids* **46**, 499 (2008).
39. Xu, D. & Chen, J. Accurate estimate of turbulent dissipation rate using piv data. *Exp. Therm. Fluid Sci.* **44**, 662–672 (2013).
40. Pope, S. B. *Turbulent Flows* (Cambridge Univ. Press, 2000).
41. Cekli, H. E., Tipton, C. & van de Water, W. Resonant enhancement of turbulent energy dissipation. *Phys. Rev. Lett.* **105**, 044503 (2010).
42. Verschoof, R. A., te Nijenhuis, A. K., Huisman, S. G., Sun, C. & Lohse, D. Periodically driven Taylor–couette turbulence. *J. Fluid Mech.* **846**, 834–845 (2018).
43. von der Heydt, A., Grossmann, S. & Lohse, D. Response maxima in modulated turbulence. *Phys. Rev. E* **67**, 046308 (2003).
44. von der Heydt, A., Grossmann, S. & Lohse, D. Response maxima in modulated turbulence. II. Numerical simulations. *Phys. Rev. E* **68**, 066302 (2003).
45. Kuczaj, A. K., Geurts, B. J. & Lohse, D. Response maxima in time-modulated turbulence: direct numerical simulations. *Europhys. Lett.* **73**, 851 (2006).
46. Lohse, D. Periodically kicked turbulence. *Phys. Rev. E* **62**, 4946 (2000).
47. Crow, S. C. & Champagne, F. Orderly structure in jet turbulence. *J. Fluid Mech.* **48**, 547–591 (1971).
48. Kraichnan, R. H. Helical turbulence and absolute equilibrium. *J. Fluid Mech.* **59**, 745–752 (1973).
49. Alexakis, A. Helically decomposed turbulence. *J. Fluid Mech.* **812**, 752–770 (2017).
50. Xavier, R. P., Teixeira, M. A. & da Silva, C. B. Asymptotic scaling laws for the irrotational motions bordering a turbulent region. *J. Fluid Mech.* **918**, A3 (2021).
51. Bisset, D. K., Hunt, J. C. & Rogers, M. M. The turbulent/non-turbulent interface bounding a far wake. *J. Fluid Mech.* **451**, 383–410 (2002).
52. Westerweel, J., Fukushima, C., Pedersen, J. M. & Hunt, J. Momentum and scalar transport at the turbulent/non-turbulent interface of a jet. *J. Fluid Mech.* **631**, 199–230 (2009).

53. Chauhan, K., Philip, J., De Silva, C. M., Hutchins, N. & Marusic, I. The turbulent/non-turbulent interface and entrainment in a boundary layer. *J. Fluid Mech.* **742**, 119–151 (2014).
54. da Silva, C. B., Dos Reis, R. J. & Pereira, J. C. The intense vorticity structures near the turbulent/non-turbulent interface in a jet. *J. Fluid Mech.* **685**, 165–190 (2011).

Methods

Additional information on the methods can be found in Supplementary Section II.

Experimental chamber and actuation

The experimental chamber was fabricated by using a commercial 3D printer with ultraviolet-cured polymers (Objet VeroWhite and VeroBlack, Objet Connex 350, Stratasys), and was primarily used throughout the experiments. A windowed chamber made of acrylic with a similar geometry was also used to measure properties of vortex rings. See Supplementary Information for the design and the exact dimensions. An electric linear actuator (Copley Controls) controls the motion of the acrylic piston through signals output from a data acquisition board (PCI-6251, National Instruments). As the piston attached to the top surface lifts up, fluid gets pulled into the chamber through the orifices, creating eight vortex rings travelling towards the centre. A rubber flap attached to the top surface around the piston's entry point prevents unwanted flow in or out of the chamber near the piston. We use a transmissive optical encoder (EM2, US Digital) to track the motion of the piston with sub-millimetre precision. With the tracking data, we extract two important parameters regarding the properties of the vortex rings: the formation number L/D(ref. 55) (that is, the stroke ratio normalized by the orifice diameter) and the effective velocity of the piston v_{eff} (Supplementary Section II). The former governs the radius and the stability of the generated vortex ring, and is a function of the diameter of the orifices D_{o} and that of the piston D_{p}. The latter controls the speed of the vortex ring. To generate two sizes of vortex rings ($R_{\mathrm{ring}} \approx 15$ mm, 25 mm), we used two settings: (D_{p}, D_{o}) = (160.0 mm, 25.6 mm) and (56.7 mm, 12.8 mm). The first setting offers a large blob of turbulence, suited for turbulent analysis through 2D particle image velocimetry. The second setting offers a blob of turbulence small enough with respect to the illuminated volume for 3D PTV to conduct the 3D flux measurements for Fig. 4 without clipping the blob. We tested effects of the different thickness of the orifices on the generated rings but found that it did not qualitatively affect the dynamics.

Velocity field extraction

To characterize the flow, we illuminated fluorescent polyethylene microspheres (diameter $d = 100$ µm, density $\rho = 1.090$ g cc^{-1}; Cospheric) with a Nd:YLF single-cavity diode-pumped solid-state laser (<40 mJ per pulse, 527 nm). A high-speed camera captured the beads' motion (Phantom v2515 or Phantom VEO4k, Vision Research) on a thin laser sheet (thickness 1 mm) for 2D PIV. We varied the frame rate of the cameras, depending on the speed of the vortex ring, ranging from 250 to 3,000 fps, while a 'quarter rule'[56] was always satisfied for the largest displacement observed. We extracted the velocity fields by using DaVis software (LaVision, Inc.), applying the pyramid algorithm[57] to generate a velocity field for turbulent analysis (energy spectrum, structure function, dissipation rate and turbulence length scales) as it was shown to extract the small-scale motion more accurately than the standard cross-correlational algorithm (Window Distortion Iterative Multigrid method[58]).

For 4D measurements, we set up an array of three to four cameras to capture the motion of the same beads illuminated in a volume of 120 mm × 100 mm × 80 mm, created by two cylindrical lenses. The 3D particle tracking algorithm called 'shake the box'[59] detected $O(10^5)$ particles from the images of the different perspectives, and reconstructed their trajectories. Binning the Lagrangian velocities gave the underlying Eulerian velocity field at that frame. On average, three to seven trajectories were present in each voxel with a width of 2.9 mm. For the voxels with no trajectories, the velocity field was interpolated linearly or filled with the neighbouring values.

3D visualization

The Lagrangian trajectories obtained by 3D PTV were first characterized by their lifespan, travelled distance, average speed and position when first detected. We used this information to identify the particles transported by the vortex rings. The selected particles were then visualized as pathlines using Houdini rendering software (SideFX). The Supplementary Videos show the pathlines combined of the four recordings for each experiment (coherent reconnections and a turbulent state).

For the visualization of the mean flow energy, the mean turbulent energy and the Q-criterion, we used Dragonfly software (Object Research Systems).

Data availability

The data contained in the plots within this paper and other findings of this study are available from the corresponding author on reasonable request.

Code availability

The codes to handle 2D PIV and 3D PTV data, to compute energy spectra, structure functions and dissipation from velocity fields, and to visualize flows are available from the corresponding author upon reasonable request.

References

55. Gharib, M., Rambod, E. & Shariff, K. A universal time scale for vortex ring formation. *J. Fluid Mech.* **360**, 121–140 (1998).
56. Raffel, M. et al. *Particle Image Velocimetry: A Practical Guide* (Springer, 2018).
57. Sciacchitano, A., Scarano, F. & Wieneke, B. Multi-frame pyramid correlation for time-resolved PIV. *Exp. Fluids* **53**, 1087–1105 (2012).
58. Scarano, F. Iterative image deformation methods in piv. *Meas. Sci. Technol.* **13**, R1 (2001).
59. Schanz, D., Gesemann, S. & Schröder, A. Shake-the-box: Lagrangian particle tracking at high particle image densities. *Exp. Fluids* **57**, 70 (2016).

Acknowledgements

We thank N. Goldenfeld, G. Voth, F. Coletti and P. A. Davidson for insightful discussions and feedback and F. Coletti and L. Baker for discussion on the performance of PIV. We thank L. Biferale and F. Bonaccorso for sharing the simulation data of helical turbulence with us via the Smart-TURB database, as well as the Turbulence Research Group at Johns Hopkins University for access to the Johns Hopkins Turbulence Database. We also acknowledge Y. Ganan and R. Morton for help in performing the Gross-Pitavskii equation simulations. This work was supported by the Army Research Office through grant nos. W911NF-17-S-0002, W911NF-18-1-0046 and W911NF-20-1-0117, and by the Brown Science Foundation. We also acknowledge LaVision Inc. for support with PIV and PTV, and SideFX and Object Research Systems for granting software licences (for Houdini and Dragonfly, respectively) to visualize flows. The Chicago MRSEC is gratefully acknowledged for access to its shared experimental facilities (U.S. NSF grant DMR2011854). For access to computational resources, we thank the University of Chicago's Research Computing Center and the University of Chicago's GPU-based high-performance computing system (NSF DMR-1828629).

Author contributions

W.T.M.I. initiated and supervised research. S.P. designed chamber actuation and performed proof of concept experiments. N.P.M. contributed to chamber design and contributed analytical tools. T.M. constructed the apparatus and the imaging system, performed all experiments reported in this paper and wrote the code to handle, process and visualize flow data. T.M. and W.T.M.I. designed experiments, analysed data, performed modelling and wrote the paper.

Competing interests

The authors declare no competing interests.

Additional information

Supplementary information The online version contains supplementary material available at https://doi.org/10.1038/s41567-023-02052-0.

Correspondence and requests for materials should be addressed to William T. M. Irvine.

Peer review information *Nature Physics* thanks Van Luc Nguyen and the other, anonymous, reviewer(s) for their contribution to the peer review of this work.